SCIENTIFIC REPORTS

OPEN

A suitable (wide-range + linear) temperature sensor based on Tm^{3+} ions

Received: 21 August 2017
Accepted: 11 October 2017
Published online: 26 October 2017

A. R. Zanatta[1], D. Scoca[2] & F. Alvarez[2]

Future advances in the broad fields of photonics, (nano-)electronics or even theranostics rely, in part, on the precise determination and control, with high sensitivity and speed, of the temperature of very well-defined spatial regions. Ideally, these temperature-sensors (T-sensors) should produce minimum (or no) disturbance in the probed regions, as well as to exhibit good resolution and significant dynamic range. Most of these features are consistent with the sharp and distinctive optical transitions of trivalent rare-earth (RE^{3+}) ions that, additionally, are susceptible to their local environment and conditions. Altogether, these aspects form the basis of the present work, in which we propose a new T-sensor involving the light emission of trivalent thulium ions (Tm^{3+}) embedded into crystalline TiO_2. The optical characterization of the TiO_2:Tm^{3+} system indicated a Tm^{3+}-related emission at ~676 nm whose main spectral features are: (1) a temperature-induced wavelength shift of $-2.2\,pm\,K^{-1}$, (2) a rather small line-width increase over the ~85–750 K range, and (3) minimum data deconvolution-processing. The study also included the experimental data of the well-established pressure- and T-sensor ruby (Al_2O_3:Cr^{3+}) and a comprehensive discussion concerning the identification and the excitation-recombination mechanisms of the Tm^{3+}-related transitions.

Along with its fairly intuitive (though not simple) concept, the physical quantity temperature is present in most of the processes taking place in real world – with exceptional examples ranging from the atomic to the outer-space environments[1,2]. Indeed, temperature is essential in many biological-chemical-physical processes influencing their activation-maintenance-interruption and, most importantly, determining their efficiency and final products[3]. Notwithstanding its omnipresence and importance, there is no universal temperature sensor (T-sensor) that comply with the specificities of all (or most of) the probed objects in terms of: range, sensitivity, precision, time response, spatial resolution, and degree of interference, for example.

T-sensors can be separated into primary or secondary systems as they provide absolute temperature values (following state equations, for example) or rely on previous calibration, respectively. Both of them derive from T-induced variations of specific materials properties such as those involving: physical aspects (dimensions, pressure, velocity, density), electrical characteristics (resistance, difference of potential, Seebeck or Peltier effects), optical radiation (light absorption-emission-polarization, index of refraction, blackbody emission), and magnetic features (chemical shift, susceptibility)[4]. Within these, modern applications require T-sensors able to provide non-contact temperature measurements of regions down to the micrometer range[5,6], as well as reliability, high sensitivity, speed, and linearity over a considerable temperature range[7]. Most of the above aspects are fulfilled by the optically-based methods, in which the temperature can be achieved by means of spectral analysis (wavelength position, intensity, shape, width, lifetime, or polarization dependence) of certain optical transitions.

A classical example of such optically-based T-sensor is ruby (Al_2O_3 doped with Cr^{3+} ions) that is a standard pressure-sensor as well[8,9]. For that purpose, the light emission at ~693 nm (corresponding to the R_1 transition of Cr^{3+} ions) is frequently used[10], rendering quite impressive wavelength shifts, *i.e.*: $\Delta\lambda_{R_1}(T) = +7.7\,pm\,K^{-1}$ [8], and $\Delta\lambda_{R_1}(P) = +36.5\,pm\,kbar^{-1}$ [11]. Even though these outstanding figures and widespread use, as far as temperature measurements are concerned, the spectral features provided by ruby crystals lack from good linearity and spatial resolution. More specifically, R_1 ruby-related wavelength shift is linear only in the ~300–600 K range[8], and no successful temperature-mapping (or -imaging) experiments were reported to date.

[1]Instituto de Física de São Carlos, USP, São Carlos, 13560-970, SP, Brazil. [2]Instituto de Física Gleb Wataghin, UNICAMP, Campinas, 13083-859, SP, Brazil. Correspondence and requests for materials should be addressed to A.R.Z. (email: zanatta@ifsc.usp.br)

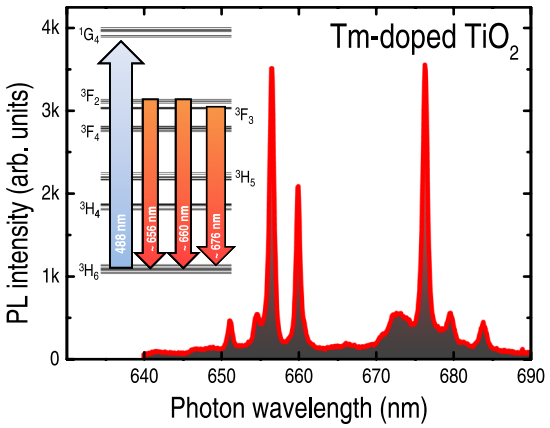

Figure 1. Photoluminescence (PL) spectra of a Tm-doped crystalline TiO_2 sample. The spectrum was achieved at room-temperature (298 K) by exciting the sample with 488.0 nm photons (~2 mW μm^{-2} power density). The inset contains a simplified energy levels diagram of the Tm^{3+} ion illustrating its optical excitation (488.0 nm) and transitions at ~656, 660, and 676 nm.

In addition to ruby, other optically-based T-sensors include the use of organic dyes[12,13], semiconductor quantum-dots[14,15], rare-earth ions[16–19], and luminescent (bio-)polymers[20,21], for example. As expected, each of the above T-sensors are best suited for a specific range of temperatures and their sensitivities depend on the optical spectrum characteristics (Table 2 of ref.[5], for example, presents an excellent overview with the typical sensitivities and range of temperatures of most of the above T-sensors).

Within this context, the T-sensors based on rare-earth ions are of special importance because of features such as: constant thermal sensitivity (as denoted by a linear behavior over a considerable range of temperatures), and no photo-degradation nor stability problems (in contrast to organic-based materials and quantum-dot structures). Furthermore, the list of rare-earth ions allows different options of photon excitation-emission (practically along the entire UV-VIS-NIR range), and compatibility with various classes of (in)organic materials (in the form of solids, liquids, nano- or micro-composites etc.) that, traditionally, have been considered for the development of rare-earth-based light-emitting sources. This is particularly true for trivalent thulium (Tm^{3+}) ions that, so far, had presented laser action at multiple wavelengths[22,23], as well as a few examples of their potential as a T-sensor[24]. In this last case, however, the T-sensor was based on the lifetime decay of the Tm^{3+}-related integrated signal in the 1000–1700 nm NIR region, after excitation with 800 nm photons. According to the experimental results, excellent fluorescence stability and good temperature sensitivity (~3 $\mu s\ K^{-1}$), in the ~298–1675 K range, were achieved from a Tm^{3+}-doped YAG (or $Y_3Al_5O_{12}$) optical fiber[25,26].

Despite the use of Tm^{3+} ions, we adopted a completely different approach in the present contribution. More specifically: the optically-active Tm^{3+} ions were embedded into a crystalline TiO_2 film, and the desired temperature was determined from the shift experienced by the Tm^{3+}-related emission at ~676 nm. Moreover: such wavelength shift proved to be rather linear (-2.2 pm K^{-1}) in the ~85–750 K range, and required almost no spectra deconvolution-analysis. Because this is the first time the wavelength shift of the Tm^{3+}-related is being proposed as a T-sensor, the work also contains a comprehensible discussion involving the main optical excitation-recombination mechanisms of the Tm^{3+} ions. A few practical applications that could be benefited from the present Tm^{3+}-based T-sensor are outlined as well.

Results and Discussion

The photoluminescence (PL) spectrum of the TiO_2:Tm^{3+} sample is displayed in Fig. 1 The spectrum was obtained at room-temperature by exciting the sample with 488.0 nm photons, and shows three Tm^{3+}-related optical transitions in the 640–690 nm wavelength range, along with a Tm^{3+} energy levels diagram (inset of Fig. 1).Considering the absence of spectroscopic data of Tm^{3+} ions in the TiO_2 matrix, the present PL assignment was based on previous works involving Tm^{3+} embedded into YCl_3[27] and $KYb(WO_4)_2$ crystals[28]. Furthermore, for simplicity reasons, only three Stark levels have been assumed, which were associated to the lowest (index 0), central (index 1), and highest (index 2) energy values found in the studies of YCl_3:Tm^{3+} and $KYb(WO_4)_2$:Tm^{3+}. According to this procedure, the main PL lines observed in Fig. 1 are due to the following transitions: $^3F_{2,2} \rightarrow {}^3H_{6,2}$ (at ~656 nm), $^3F_{2,0\text{-}1} \rightarrow {}^3H_{6,2}$ (at ~660 nm), and $^3F_{3,0\text{-}1} \rightarrow {}^3H_{6,0\text{-}1}$ (at ~676 nm) [Supplementary Figure S1]. Likewise, the photon excitation with 488.0 nm photons is quasi-resonant with the $^3H_{6,0\text{-}2} \rightarrow {}^1G_{4,0\text{-}2}$ transition.

In addition to these, other optical emissions were observed in the 500–850 nm interval: either due to Tm^{3+} ions (at ~560 and 790 nm, ascribed to the $^3F_3 \rightarrow {}^3H_5$, and $^1G_4 \rightarrow {}^3H_5$ or $^3F_4 \rightarrow {}^3H_6$ transitions, respectively), or originating from the TiO_2 matrix (>800 nm)[29].

As indicated by the room-temperature spectrum of Fig. 1, the Tm^{3+}-related optical emissions are well-defined, background-free, and rather sharp. Nonetheless, the most remarkable feature of the Tm^{3+}-related signal involves the temperature-induced wavelength shift of the $^3F_{3,0\text{-}1} \rightarrow {}^3H_{6,0\text{-}1}$ (at ~676 nm) transition, without major changes in the overall spectrum (Fig. 2). Such behavior is in contrast with that exhibited by the traditional optically-based T-sensor ruby[8], for example, in which case the spectral line-width and, consequently, temperature precision are highly affected at increasing temperatures.

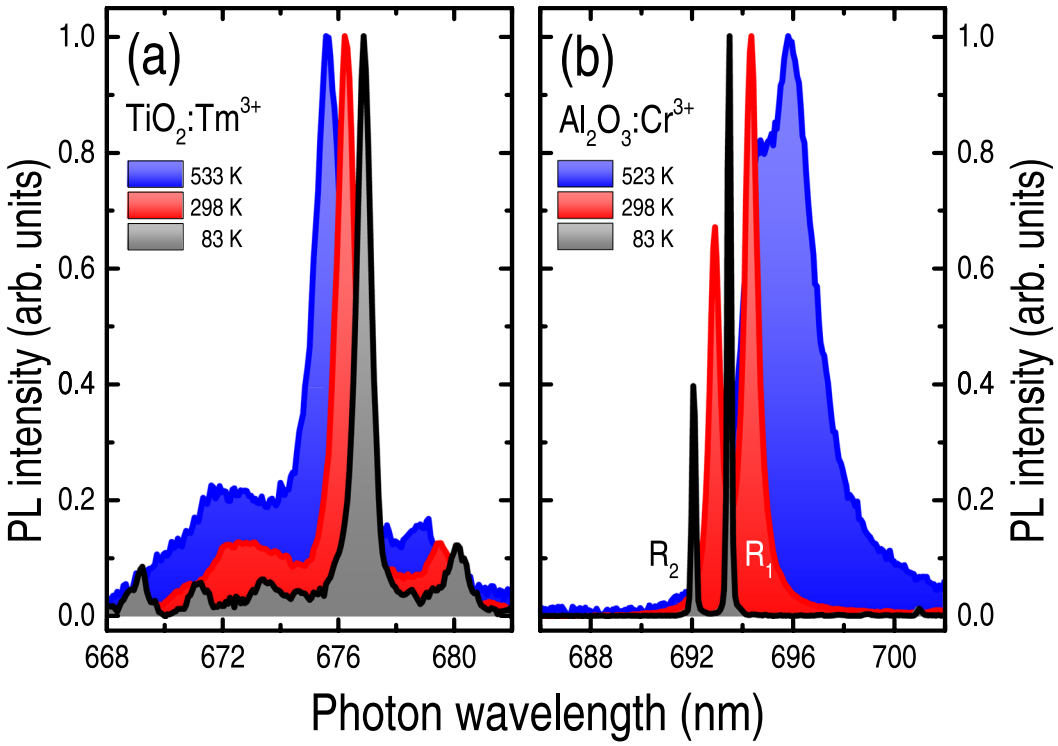

Figure 2. Photoluminescence spectra (taken at the temperatures indicated in the figure) of: (**a**) a Tm-doped TiO_2 sample, and (**b**) natural ruby (Al_2O_3:Cr^{3+}) crystal. All measurements were performed after keeping the samples at the desired temperature for ~2 min. The spectra were normalized for comparison purposes. Notice the spectral changes (wavelength and line-width) experienced by the Tm^{3+}- and Cr^{3+}-related transitions as induced by the temperature of measurement.

The analysis of the Tm^{3+}-related PL(T) spectra indicate that the $^3F_{3,0\text{-}1} \rightarrow {}^3H_{6,0\text{-}1}$ transition experienced a linear, wavelength shift $d\lambda/dT$ of $-2.2\,pm\,K^{-1}$ (or $+0.048\,cm^{-1}\,K^{-1}$), with a 1.25 nm (or $55\,cm^{-1}$) line-width increase, along the entire ~85–750 K measured range. Also, the PL signal intensity I_{PL} changed for only two orders of magnitude and the spectral analysis required almost no data processing, except for the fitting of a Lorentzian function to the $^3F_{3,0\text{-}1} \rightarrow {}^3H_{6,0\text{-}1}$ transition signal [Supplementary Figure S2].

Analogously, for the R_1 and R_2 ruby lines (measured and analyzed in the very same way): (1) the wavelength shifts were higher ($+7.7\,pm\,K^{-1}$ or $-0.16\,cm^{-1}\,K^{-1}$), but presented a linear behavior only in the ~300–600 K interval, (2) from ~85 to 750 K, the corresponding line-widths increase were R_1 ~ 6.8 nm (or $280\,cm^{-1}$) and R_2 ~ 2.6 nm (or $109\,cm^{-1}$), (3) the I_{PL} signal experienced a three orders of magnitude variation, and (4) above ~400 K there was a considerable overlapping of the R_1-R_2 lines which influenced the wavelength accuracy [Supplementary Figure S3].

Most of the above features are displayed in Figs 3 and 4, in which the error bars took into account: the experimental resolution (~$1\,cm^{-1}$), different measurement runs, and data processing-analysis (involving changes due to background removal, for example).

Figure 3 shows the peak wavelength of the Tm^{3+} and Cr^{3+} ions, as experimentally determined in the ~85–750 K range. The figure also presents the mathematical fittings of the Tm^{3+}-related experimental data [$\lambda_{Tm^{3+}}(T) = 676.9 - 2.2 \times 10^{-3}\,T\,nm$], as well as those obtained by Ragan *et al.*[8] in ruby [$\lambda_{R_1}(T) = 693.34 - 2.17 \times 10^{-3}\,T + 2.31 \times 10^{-5}\,T^2 - 1.78 \times 10^{-7}\,T^3$ nm and $\lambda_{R_2}(T) = 691.94 - 1.44 \times 10^{-3}\,T + 1.86 \times 10^{-5}\,T^2 - 1.21 \times 10^{-8}\,T^3$ nm – in the 0–300 K interval]. Not only the gradient and linearity of the curves are different but, interestingly, the wavelength shifts presented by both ions are contrary: negative for Tm^{3+} ions (blue-shift), and positive for Cr^{3+} (red-shift).

All of these characteristics derive from the properties of each ion as well as from the ion-host interaction and, part of them, were reported in the literature[30–32]. Basically, when embedded into a crystal host, impurities (like the Tm^{3+} or Cr^{3+} ions, for example) move around their equilibrium positions giving rise to lattice vibrations. Optical transitions between any two levels of these impurities can be brought about in, at least, two ways: (a) a direct or electron-phonon EP process (transition from one level to another such that any energy difference is compensated by phonon absorption or emission, to allow the transition), and (b) a Raman process (the transition is made possible by energy variations due to phonon scattering).

As expected, both EP and Raman processes are dependent on temperature and, ultimately, affects the wavelength and line-width of the transitions. In the former case, the T-induced wavelength shifts are associated with variations of the crystal field energy because of local lattice vibrations. In the latter, the line-width changes as a result of the transitions between the crystal field levels stimulated by interaction with the acoustical phonon field. Roughly, the T-induced variations in the spectral characteristics of any transition can be described by[31]:

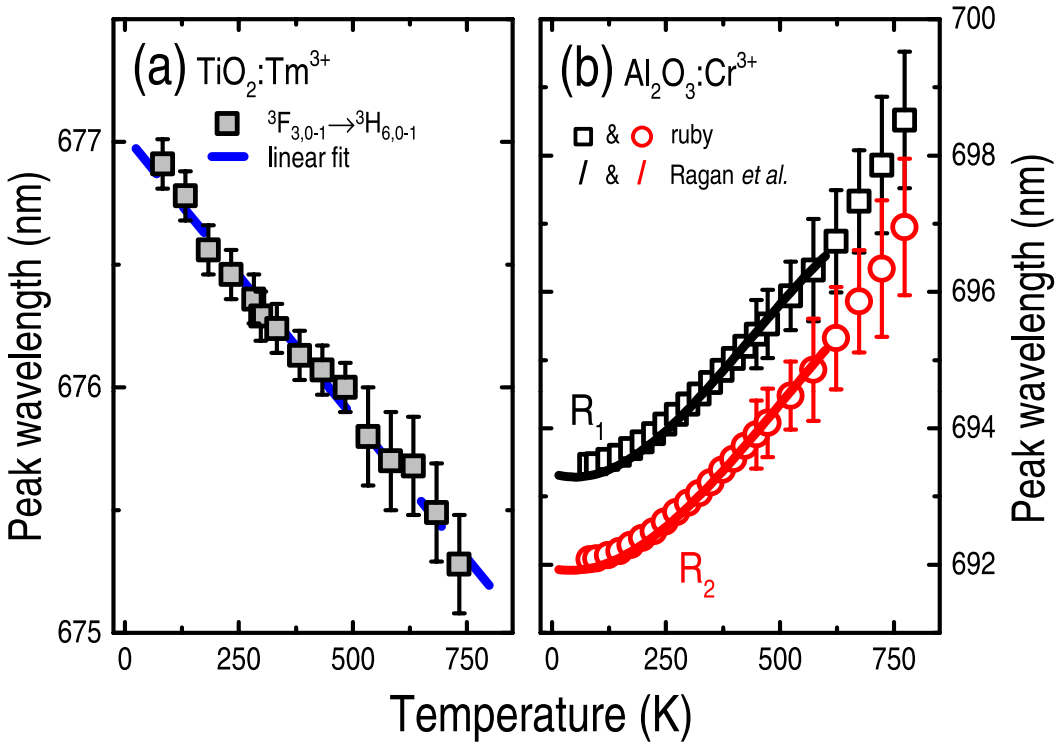

Figure 3. Peak wavelength as a function of temperature (~85–750 K) due to: (**a**) Tm^{3+} ions embedded into crystalline (Anatase) TiO_2 films ($^3F_{3,0\text{-}1} \rightarrow {}^3H_{6,0\text{-}1}$ transition), and (**b**) Cr^{3+} ions embedded into ruby or Cr-doped Al_2O_3 crystal (R_1 and R_2 lines corresponding to the $^2E \rightarrow {}^4A_2$ transition). All points refer to experimental data obtained in the present work. The dashed blue (solid black and red) lines account for the mathematical fitting of the experimental data (the expression given by Ragan *et al.*[8]). The error bars comprise uncertainties due to experimental acquisition and data analysis.

$$E(T) = E(0) + E_{direct}(T) + E_{Raman}(T) \text{ and } \Gamma(T) = \Gamma(0) + \Gamma_{direct}(T) + \Gamma_{Raman}(T) \quad (1)$$

where E and Γ stand for the energy and line-width of the transition, respectively. Moreover: the first terms [E(0) and Γ(0)] account for the T-independent or static-like interactions (crystal field interaction, nephelauxetic effect, strain-stress, for example), the index "direct" stand for the direct processes (EP interactions and those ones associated with non-harmonic effects like thermal expansion-compression[33]), and the index "Raman" denotes the processes involving the scattering of phonons. The formal description of the E(T) and Γ(T) quantities are based on the Hamiltonian of the impurity-phonon system and the Debye model for the phonon distribution. It involves a lot of adjustable-unknown parameters and, in most of the cases, it reproduces the experimental results at the expense of unreliable-conflicting values (Debye temperature and phonon frequency different from those available in literature, different coupling factors for the very same transition, different E(0) and Γ(0) values for the very same material etc.).

In spite of this limitation, the model is very instructive to indicate the origin of the observed red- and blue-shifts. According to the model, the red-shift is typical of impurity–matrix systems in which the EP interactions and/or phonon scattering processes are predominant, as verified in ruby (Al_2O_3:Cr^{3+})[30], and YAG:Cr^{3+} [34]. Blue-shifts, on the contrary, are typical of the rare-earth ions because of the strong non-harmonic influence[31,33,35,36]. In fact, the primacy of the EP interactions and/or phonon-scattering processes are consistent with the great changes observed in the I_{PL} and line-width of the Cr^{3+}-related transitions [Fig. 4(c,d)], that are also susceptible to strain-stress and concentration details[37].

Concerning the peculiar I_{PL} behavior presented by the TiO_2:Tm^{3+} sample [Fig. 4(a)], it originates because of variations in the energy of the Tm^{3+} levels and the quasi-resonant photon excitation process. More precisely, I_{PL} is highest when photon absorption is maximum, *i.e.*, around room-temperature due to the almost perfect match between the $^3H_{6,0\text{-}2} \rightarrow {}^1G_{4,0\text{-}2}$ transition and the 488.0 nm photon energy. Below, or above, room-temperature the energy of the $^1G_{4,0\text{-}2}$ levels change such that the photon absorption process is incomplete, rendering some decrease of I_{PL}. Likewise, the T-induced energy variation of certain levels is the origin of the wavelength shift values presented by the Tm^{3+} and Cr^{3+} ions.

Despite their inherent energy levels arrangement, both Tm^{3+} and Cr^{3+} ions are influenced by their local atomic surroundings which, in essence, are decided by external agents like temperature, pressure, electromagnetic fields etc. Such ion–host correlation is usually expressed in terms of the crystalline-field theory, that has been extensively considered in the study of rare-earth (RE) and transition-metal (TM) ions[38,39].

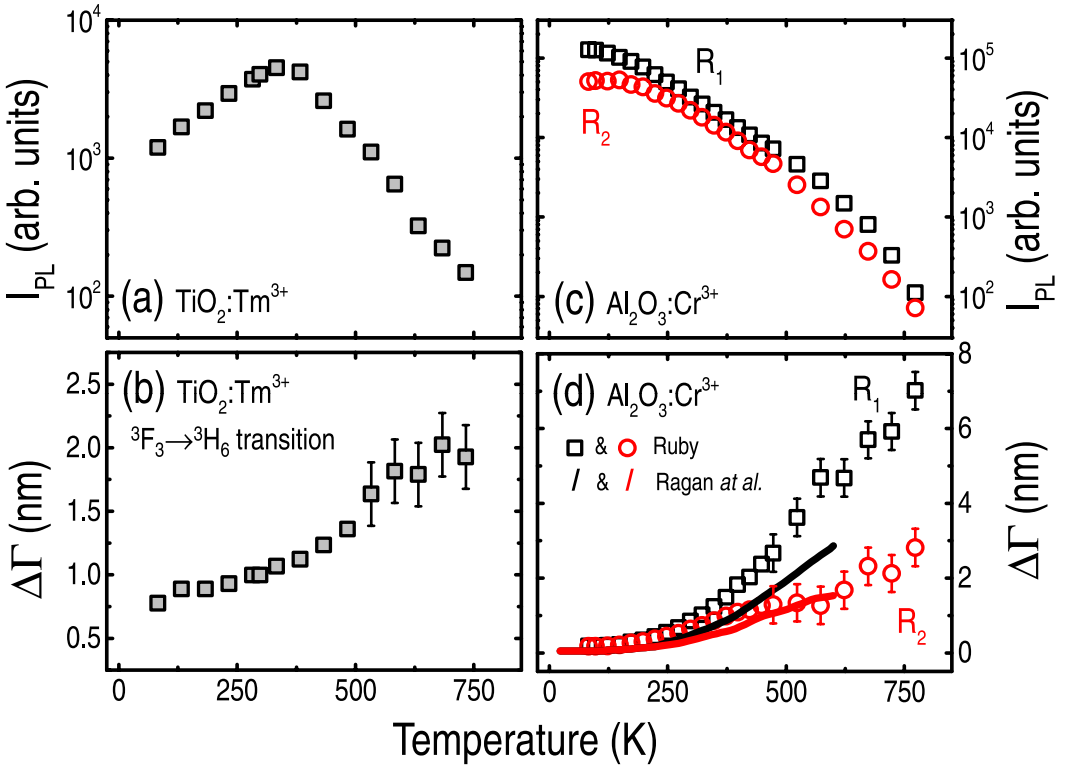

Figure 4. Photoluminescence intensity (I_{PL}) and transition line-width ($\Delta\Gamma$), in the ~85–750 K temperature range, due to: (**a**,**b**) Tm^{3+} ions ($^3F_{3,0\text{-}1} \rightarrow {}^3H_{6,0\text{-}1}$ transition), and (**c**,**d**) Cr^{3+} ions (R_1 and R_2 lines corresponding to the $^2E \rightarrow {}^4A_2$ transition). All points refer to data obtained in the present work, following 488.0 nm excitation (~2 mW μm^{-2} power density). The black and red solid lines refer to the expression given by Ragan *et al.*[8]. Error bars took into account uncertainties involving spectra acquisition and data analysis.

According to this approach, $RE^{3+/2+}$ ions appear to be the less affected by the so-called crystalline-field effects. It happens because of the outer 5 s and 5p orbitals that partially shield the intra-4f transitions of the RE^{3+} or RE^{2+} ions – in contrast to the TM^{3+}-related transitions that take place at the vulnerable 3d orbitals. Nonetheless, the local atomic environment changes the $RE^{3+/2+}$-related transitions, and its final effects can be enhanced depending on the ion–host characteristics, as verified in this work.

Based on the present experimental results, the wavelength-shift experienced by Tm^{3+}, at ~676 nm, corresponds to almost 30% that of Cr^{3+}. The wavelength-shifts of the other Tm^{3+}-related transitions (at ~656 and 660 nm) are well-defined and linear as well, but presented a smaller rate: $d\lambda/dT$ ($^3F_{2,2} \rightarrow {}^3H_{6,2}$) = $d\lambda/dT$ ($^3F_{2,0\text{-}1} \rightarrow {}^3H_{6,2}$) = −1.1 pm K^{-1} [Supplementary Figure S4]. These figures not only are consistent with the crystalline-field theory (in the sense that $RE^{3+/2+}$ ions are less sensitive than TM^{3+} ions), but are similar to those achieved from other $RE^{3+/2+}$ ions: Eu^{3+} in YAG with $d\lambda/dt = -0.5$ pm K^{-1} (or +0.015 cm^{-1} K^{-1}) and a linear 293–1073 K range[40]; Sm^{3+} in YAG with $d\lambda/dt = -0.7$ pm K^{-1} (or +0.018 cm^{-1} K^{-1}) and a linear 300–873 K range[36]; Sm^{3+} in TiO_2 with $d\lambda/dt = -0.7$ pm K^{-1} (or +0.017 cm^{-1} K^{-1}) and a linear 83–750 K range[41] [Supplementary Figure S5]; Sm^{2+} in SrB_4O_7 with $d\lambda/dt = -0.1$ pm K^{-1} (or +0.002 cm^{-1} K^{-1}) and a linear 293–673 K range[42]. The only exception to these values applies to the Tm^{3+}-related transition at ~676 nm, in which $d\lambda/dT = -2.2$ pm K^{-1} (or +0.048 cm^{-1} K^{-1}) is, at least, 2–3 times higher than other $RE^{3+/2+}$ ions. This can be seen in Fig. 5 that shows the wavelength shifts of Tm^{3+} (at ~676 nm), Sm^{3+} (one of those exhibiting the highest slopes amongst the RE ions, at ~612 nm), and Cr^{3+} ions (representing the standard optically-based T-sensor).

Within the possible reasons that explain the wavelength-shift presented by the TiO_2:Tm^{3+} sample we can mention: (a) the arrangement of Tm^{3+}-related energy levels, as imposed by the TiO_2 host; and (b) the TiO_2 host in the form of a thin film, aggregating to the already existing T-induced crystalline-field and non-harmonic effects, those ones due to the T-induced film-substrate interaction. Though reasonable, the film-substrate interaction is a hypothesis that requires the systematic investigation of a bulk TiO_2:Tm^{3+} sample for validation. Therefore, the main spectroscopic features of the TiO_2:Tm^{3+} system can be summarized as: (1) TiO_2 is a wide bandgap material that is able to produce considerable field distortion around the Tm^{3+} ions; (2) the $^3F_{2,2} \rightarrow {}^3H_{6,2}$, $^3F_{2,0\text{-}1} \rightarrow {}^3H_{6,2}$, and $^3F_{3,0\text{-}1} \rightarrow {}^3H_{6,0\text{-}1}$ transitions take place at ~656, 660, and 676 nm, respectively; (3) temperature determines the crystalline-field and gives rise to non-harmonic effects like thermal compression-expansion; (4) as the temperature advances, the mutual play of these effects provokes the separation of the Tm^{3+}-related energy levels and, ultimately, the blue-shift of all transitions; and (5) optical transitions ending at the $^3H_{6,2}$ state (*i.e.*, $^3F_{2,2} \rightarrow {}^3H_{6,2}$ and $^3F_{2,0\text{-}1} \rightarrow {}^3H_{6,2}$) present a smaller blue-shift than those involving the lowest $^3H_{6,0\text{-}1}$ ground states ($^3F_{3,0\text{-}1} \rightarrow {}^3H_{6,0\text{-}1}$) – in accord with quantum mechanics principles[31].

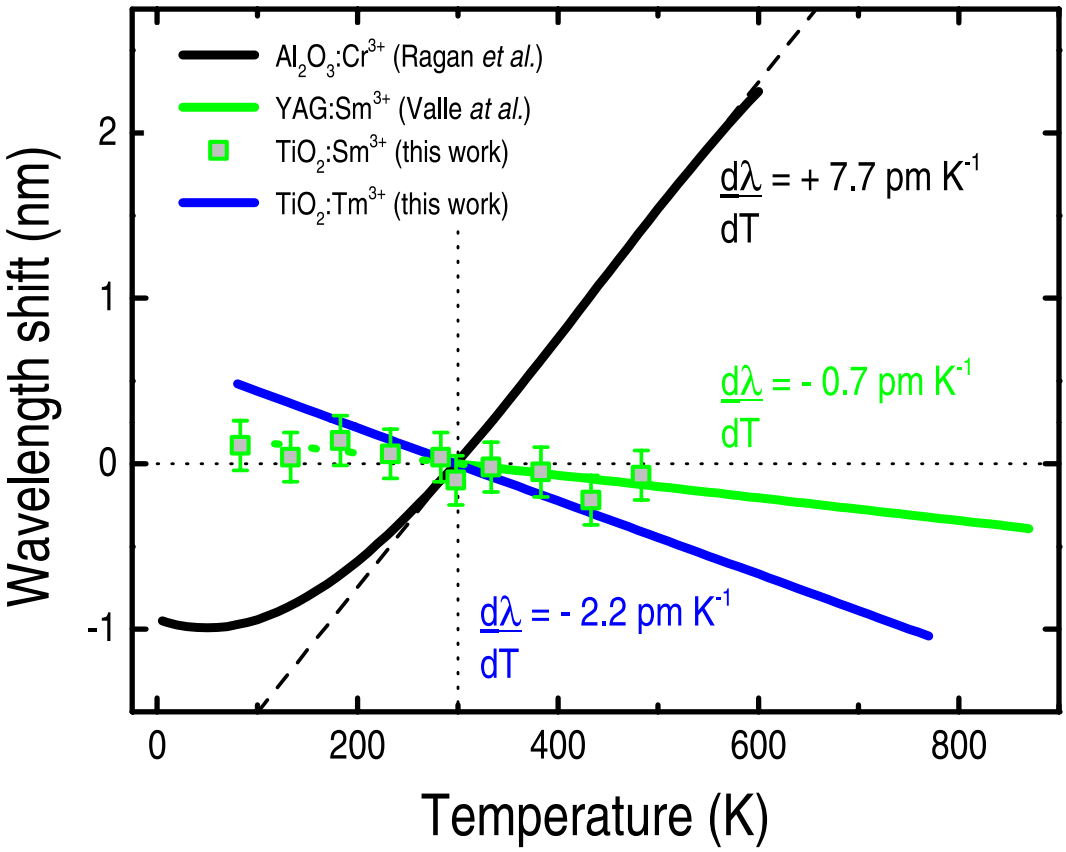

Figure 5. Wavelength shift (as referred to that verified at room-temperature) as a function of temperature due to: Cr^{3+} in ruby (experimental data of Ragan *et al.*[8]), Sm^{3+} when inserted in YAG crystals (Valle *et al.*[36]), and Sm^{3+} and Tm^{3+} ions embedded into crystalline Anatase TiO_2 films (this work). The solid lines refer to the best mathematical description of the experimental data. Along with the higher $d\lambda/dT$ exhibited by ruby, notice its modest range (~300–600 K) of linear variation.

In summary, the TiO_2:Tm^{3+} system represents a very convenient option to the ever-increasing area of optically-based temperature sensors. Along with its many interesting characteristics (linear blue-shift over a quite large T-range, visible light emission with no great line-width variation, and no need of hard spectrum processing), the system comprises the inert-biocompatible TiO_2 matrix. Indeed, the whole procedure (sample production + optical excitation/detection + spectrum analysis) involves rather simple instrumentation which, allied to its sensitivity, suggests the potential of the TiO_2:Tm^{3+} system as an suitable T-sensor in photonics, (nano-) electronics, theranostics[43–45], thermal imaging-mapping etc. Moreover, in the form of a thin film, the TiO_2:Tm^{3+} system allows its attachment (instant or permanent) to almost any solid surface – ideally in the $1–10^{-9}$ m range – without generating great temperature variations.

Concluding remarks. We reported on the use of Tm^{3+} ions as an optically-based temperature-sensor. The Tm^{3+} ions were embedded into a crystalline TiO_2 film, and the actual temperature was determined from the shift experienced by the Tm^{3+}-related emission at ~676 nm. Were applicable, the work compared the spectroscopic data of the Tm^{3+} ions with those of the well-established pressure- and T-sensor ruby (Al_2O_3:Cr^{3+}). In contrast to ruby, the experimental results indicated that the Tm^{3+}-related wavelength shift is rather linear and required almost no spectra deconvolution-analysis. Also, whereas the Cr^{3+} ions showed a red-shift of $+7.7\,pm\,K^{-1}$, the Tm^{3+} ions exhibited a smaller ($-2.2\,pm\,K^{-1}$) blue-shift, though over a considerable dynamic range (83–750 K).

We also presented a comprehensive discussion concerning the Tm^{3+}-related transitions as well as the T-induced factors that most affect their wavelength shift.

The present experimental results suggest the suitability of the TiO_2:Tm^{3+} system as an optically-based T-sensor in terms of its simplicity, sensitivity, and wide linear dynamic range. Future work, however, should consider its spatial resolution as well as its real operation in photonics, (nano-)electronics, and biological applications, for example.

Methods

The present thulium-doped TiO_2 sample was deposited onto a crystalline silicon substrate by sputtering a high purity Titanium + Thulium solid target (properly adjusted according to the Ti and Tm relative areas and sputtering yields[46]) to generate a Tm concentration around 0.5 at.%[18]. During deposition, the Ti + Tm target was bombarded by a beam of Ar^+ ions (1.5 keV and nominal current ~13 mA/cm^2) that was generated by a Kaufman cell.

The whole procedure was carried out in a high vacuum chamber under an atmosphere of pure oxygen (5×10^{-4} mbar), by keeping the crystalline silicon substrate at 473 K. Under these conditions, after 120 min, a 300 nm thick uniform film was obtained.

Subsequently, the Tm-doped TiO_2 sample was cut into 1 cm^2 pieces and one of them was annealed at 873 K under a flow of oxygen gas at atmospheric pressure, during 30 min. All samples – as-deposited and after thermal annealing – were investigated by X-ray photoelectron spectroscopy (XPS), X-ray diffraction (XRD), Raman spectroscopy, and photoluminescence (PL) experiments. Whereas the XPS analysis confirmed the presence of ~0.5 at.% of Tm in the TiO_2 films, both XRD and Raman measurements indicated their amorphous to crystalline transformation (predominantly in the Anatase phase) after thermal annealing at 873 K [Supplementary Figure S6].

The PL experiments were carried out in a commercial micro-Raman setup (Renishaw RM2000) by exciting the Tm-doped TiO_2 sample with 488.0 nm photons. The temperature-dependent spectra were obtained in the 83–773 K range by means of a computer-controlled T-stage (Linkam THMS 600). Further information concerning the sample deposition conditions (and method[47]) and characterization details can be found elsewhere[41].

For comparison purposes, a Sm-doped TiO_2 film (deposited and annealed following exactly the same procedure above described) and a natural ruby sample (Cr-doped Al_2O_3) had their photoluminescence investigated in detail. Given the high temperature sensitivity of the samples under investigation, the PL measurements were conducted at the lowest laser excitation power density (~2 mW μm^{-2}). Following this condition, all observed spectral variations (wavelength shift, line-width, and signal intensity) are exempt from experimental artifacts. Accordingly, all PL(T) measurements shared the same experimental accuracy, *i.e.*: ~1 cm^{-1} (spectral) and <0.2 K (reproducibly achieved after 2 min of thermal stabilization).

References

1. Quinn, T. J. *Temperature* Chapter 1 (Academic Press Inc., Orlando USA, 1983).
2. Chang, H. *Inventing temperature: Measurement and scientific progress* Chapters 4 and 5 (Oxford University Press, New York USA, 2004).
3. Atkins, P. W. *Physical chemistry* Chapters 2 and 3 (Oxford University Press, New York USA, 1994).
4. Schooley, J. F. *Thermometry* Chapters 5 and 6.(CRC Press Inc., Boca Raton USA, 1988).
5. Brites, C. D. S. *et al*. Thermometry at the nanoscale. *Nanoscale* **4**, 4799–4829 (2012).
6. Jaque, D. & Vetrone, F. Luminescence nanothermometry. *Nanoscale* **4**, 4301–4326 (2012).
7. Khalid, A. H. & Kontis, K. Thermographic phosphors for high temperature measurements: Principles, current state of the art and recent applications. *Sensors* **8**, 5673–5744 (2008).
8. Ragan, D. D., Gustavsen, R. & Schiferl, D. Calibration of the ruby R_1 and R_2 fluorescence shifts as a function of temperature from 0 to 600 K. *J. Appl. Phys.* **72**, 5539–5544 (1992).
9. Goncharov, A. F., Zaug, J. M. & Crowhurst, J. C. Optical calibration of pressure sensors for high pressures and temperatures. *J. Appl. Phys.* **97**, 094917–1-5 (2005).
10. Henderson, B. & Imbusch, G. F. *Optical spectroscopy of inorganic solids* Chapter 9 (Oxford University Press, New York USA, 1989).
11. Piermarini, G. J., Block, S., Barnett, J. D. & Forman, R. A. Calibration of the pressure dependence of the R_1 ruby fluorescence line to 195 kbar. *J. Appl. Phys.* **46**, 2774–2780 (1975).
12. Ross, D., Gaitan, M. & Locascio, L. E. Temperature measurement in microfluidic systems using a temperature-dependent fluorescent dye. *Anal. Chem.* **73**, 4117–4123 (2001).
13. Benninger, R. K. P. *et al*. Quantitative 3d mapping of fluidic temperatures within microchannel networks using fluorescence lifetime imaging. *Anal. Chem.* **78**, 2272–2278 (2006).
14. Vlaskin, V. A., Janssen, N., Rijssel, J. V., Beaulac, R. & Gamelin, D. R. Tunable dual emission in doped semiconductor nanocrystals. *Nano Lett.* **10**, 3670–3674 (2010).
15. Maestro, L. M. *et al*. CdSe quantum dots for two-photon fluorescence thermal imaging. *Nano Lett.* **10**, 5109–5115 (2010).
16. Carlson, M. T., Khan, A. & Richardson, H. H. Local temperature determination of optically excited nanoparticles and nanodots. *Nano Lett.* **11**, 1061–1069 (2011).
17. Gonzalez, P. H. *et al*. Evaluation of rare-earth-doped silica sub-micrometric spheres as optically controlled temperature sensors. *J. Appl. Phys.* **112**, 054702–1-7 (2012).
18. Scoca, D., Morales, M., Merlo, R., Alvarez, F. & Zanatta, A. R. Photoluminescence and compositional-structural properties of ion-beam sputter deposited Er-doped $TiO_{2-x}N_x$ films: Their potential as a temperature sensor. *J. Appl. Phys.* **117**, 205304–1-6 (2015).
19. Manzani, D., Petruci, J. F. S., Nigoghossian, K., Cardoso, A. A. & Ribeiro, S. A portable luminescent thermometer based on green up-conversion emission of Er^{3+}/Yb^{3+} co-doped tellurite glass. *Sci. Rep.* **7**, 41596–1-11 (2017).
20. Pietsch, C., Vollrath, A., Hoogenboom, R. & Schubert, U. S. A fluorescent thermometer based on a pyrene-labeled thermoresponsive polymer. *Sensors* **10**, 7979–7990 (2010).
21. Okabe, K. *et al*. Intracellular temperature mapping with a fluorescent polymeric thermometer and fluorescence lifetime imaging microscopy. *Nat. Commun.* **3**, 705–1-9 (2012).
22. Kaminskii, A. A. Laser crystals and ceramics: Recent advances. *Laser & Photon. Rev.* **1**, 93–177 (2007).
23. Wen, X. *et al*. Highly Tm^{3+} doped germanate glass and its single mode fiber for 2.0 μm laser. *Sci. Rep.* **6**, 20344–1-10 (2016).
24. Grattan, K. T. V. & Zhang, Z. Y. *Fiber optic fluorescence thermometry* (Chapman & Hall, New York USA, 1995).
25. Zhang, Z. Y., Grattan, K. T. V. & Meggitt, B. T. Thulium-doped fiber optic decay-time temperature sensors: Characterization of high temperature performance. *Rev. Sci. Instrum.* **71**, 1614–1620 (2000).
26. Shen, Y., Zhao, W., He, J., Sun, T. & Grattan, K. T. V. Fluorescence decay characteristic of Tm-doped YAG crystal fiber for sensor applications, investigated from room temperature to 1400 °C. *IEEE Sensors Journal* **3**, 507–512 (2003).
27. Dieke, G. H. *Spectra and energy levels of rare-earth ions in crystals* Chapter 13 (Wiley Interscience, New York USA, 1968).
28. Pujol, M. C. *et al*. Crystal growth and spectroscopic characterization of Tm^{3+}-doped $KYb(WO_4)_2$ single crystals. *Phys. Rev. B* **66**, 144304–1-8 (2002).
29. Montoncello, F. *et al*. Near-infrared photoluminescence in titania: Evidence for phonon-replica effect. *J. Appl. Phys.* **94**, 1501–1505 (2003).
30. McCumber, D. E. & Sturge, M. D. Linewidth and temperature shift of the R lines in ruby. *J. Appl. Phys.* **34**, 1682–1684 (1963).
31. Kushida, T. Linewidths and thermal shifts of spectral lines in Nd-doped yttrium aluminum garnet and calcium fluorophosphate. *Phys. Rev.* **185**, 500–508 (1969).
32. Hüfner, S. *Optical spectra of transparent rare-earth compounds* Chapter 4 (Academic Press Inc., New York USA, 1978).
33. Kuznetsov, A., Laissar, A. & Kikas, J. Temperature dependence of spectral position and widths of $^5D_J \rightarrow {}^7F_J$ fluorescence lines originating from Sm^{2+} ions in SrFCl crystals. *Opt. Mater.* **32**, 1671–1675 (2010).

34. Zheng, W. C., Li, B. X. & Feng, G. Y. Thermal shifts and electron-phonon coupling parameters of the R-lines for Cr^{3+} ion in $Y_3Al_5O_{12}$ crystal. *Opt. Mater.* **35**, 626–628 (2013).
35. Hess, N. J. & Schiferl, D. Pressure and temperature dependence of laser-induced fluorescence of Sm:YAG to 100 kbar and 700 °C and an empirical model. *J. Appl. Phys.* **68**, 1953–1960 (1990).
36. Valle, C. S., Daniel, I., Reynard, B., Abraham, R. & Goutaudier, C. Optimization of Sm^{3+} fluorescence in Sm-doped yttrium aluminum garnet: Application to pressure calibration in diamond-anvil cell at high temperature. *J. Appl. Phys.* **92**, 4349–4353 (2002).
37. Piermarini, G. J., Block, S. & Barnett, J. D. Hydrostatic limits in liquids and solids to 100 kbar. *J. Appl. Phys.* **44**, 5377–5382 (1973).
38. Blasse, G. & Grabmaier, B. C. *Luminescent materials* Chapters 1 & 3 (Springer-Verlag, Heidelberg GER, 1984).
39. Solé, J. G., Bausá, L. E. & Jaque, D. *An introduction to the optical spectroscopy of inorganic solids* Chapter 6 (John Wiley & Sons, Chichester UK, 2005).
40. Arashi, H. & Ishigame, M. Diamond anvil cell and pressure sensor for high-temperature use. *Jpn. J. Appl. Phys.* **21**, 1647–1649 (1982).
41. Scoca, D., Zanatta, A. R. & Alvarez, F. On the optical-electronic properties of TiO_2 films doped with Sm, Tb, and Sm + Tb. (unpublished).
42. Lacam, A. & Chateau, C. High-pressure measurements at moderate temperatures in a diamond anvil cell with a new optical sensor: SrB_4O_7:Sm^{2+}. *J. Appl. Phys.* **66**, 366–372 (1989).
43. Hao, S., Chen, G. & Yang, C. Sensing using rare-earth-doped upconversion nano-particles. *Theranostics* **3**, 331–345 (2013).
44. Naczynski, D. J. *et al.* Rare-earth-doped biological composites as *in vivo* shortwave infrared detectors. *Nat. Commun.* **4**, 2199–1-10 (2013).
45. Shen, J., Sun, L. D. & Yan, C. H. Luminescent rare-earth nano-materials for bio-probe applications. *Dalton Trans.* **42**, 5687–5697 (2008).
46. Vossen, J. L. & Cuomo, J. J. *ThinFilm Processes* Chapter II-1 (Eds Vossen, J. L. & Kern, W.) (Academic Press Inc., New York, NY 1978).
47. Hammer, P., Victoria, N. M. & Alvarez, F. Electronic structure of hydrogenated carbon nitride films. *J. Vac. Sci. Technol. A* **16**, 2941–2949 (1998).

Acknowledgements

This work was financially supported by the Brazilian agencies FAPESP (grant 2012/10127-5), CNPq (A.R.Z. and F.A.), and CAPES (D.S.).

Author Contributions

This paper is part of the D.S.'s PhD thesis. A.R.Z., D.S. and F.A. have conceived and discussed the whole experimental work. D.S. made the Tm- and Sm-doped TiO_2 samples and carried out the XPS and XRD measurements. Along with A.R.Z., D.S. performed the sample processing and Raman and PL(T) experiments. All authors contributed with the data analysis and with the writing/editing of the manuscript.

Additional Information

Supplementary information accompanies this paper at https://doi.org/10.1038/s41598-017-14535-1.

Competing Interests: The authors declare that they have no competing interests.

Publisher's note: Springer Nature remains neutral with regard to jurisdictional claims in published maps and institutional affiliations.